Materials Horizons

Benign Mid-Gap Halide Vacancy States in 2D Bismuth-Based Halide Perovskite Microcrystals for Enhanced Broadband Photodetectors

Journal:	*Materials Horizons*
Manuscript ID	MH-COM-10-2024-001532.R2
Article Type:	Communication
Date Submitted by the Author:	24-Feb-2025

Complete List of Authors:	Singh, Kuntal ; Indian Association for the Cultivation of Science Hossain, Mozakkar; Indian Association for the Cultivation of Science, School of Applied and Interdisciplinary Sciences Nayak, Pabitra; IIT Delhi, Dept Chemistry KARMAKAR, SOUGATA ; Indian Association for the Cultivation of Science, Applied and Interdisciplinary Sciences Tripathi, Akash ; Indian Institute of Science Education and Research Bhopal, Physiscs Sarkar, Prakash; Indian Association for the Cultivation of Science, Applied and Interdisciplinary Sciences Rudra, Pratyasha; CSIR-Central Glass and Ceramic Research Institute Muhammed Ali, A V; Centre for Nano and Soft Matter Sciences, Grandhi, G. Krishnamurthy; Tampere University, ; Vivo, Paola; Tampere University, Mondal, Swastik; CSIR-Central Glass and Ceramic Research Institute, ; Adarsh, K.; Indian Institute of Science Education and Research Bhopal, Physiscs Ghosh, Dibyajyoti; IIT Delhi, Rao, K.; Indian Association for the Cultivation of Science, Applied and Interdisciplinary Sciences

This work introduces a novel defect-engineering strategy in 2D bismuth-based halide perovskite-inspired materials (Bi-PIMs) by deliberately incorporating iodine vacancies to create benign mid-gap states in $Cs_3Bi_2Br_3I_{5.2}$ microcrystals (MCs). Unlike conventional approaches, which aim to eliminate defects, we demonstrate that iodine vacancies can be harnessed to improve charge transport and extend the photoresponse beyond the intrinsic bandgap. Interestingly, theoretical models of lead halide perovskites suggest that iodine vacancies may not induce significant non-radiative recombination, implying a potential for defect tolerance. However, the experimental control and quantification of these vacancies in thin films remain challenging due to grain boundaries and interface effects. Our study overcomes these challenges in 2D-$Cs_3Bi_2Br_3I_{5.2}$ MCs by utilizing vacancy-induced mid-gap states to maintain efficient band-edge exciton behavior while facilitating n-type doping, improving carrier mobility and reducing recombination losses. This approach sets our work apart from existing research by demonstrating how vacancies can actively tune the spectral response, enhancing performance in self-powered photodetectors across a broad wavelength range (400-800 nm). This concept provides new insights into the relationship between vacancy-induced mid-gap states and the quasi-direct bandgap nature of Bi-PIMs, opening new pathways for creating efficient, lead-free, and low-toxicity optoelectronic devices such as photodetectors and solar cells.

Data Availability Statement

The data supporting the findings of this study are available within the manuscript and its supplementary information files. Any additional raw data required to reproduce the findings can be made available upon reasonable request from the corresponding author, Dr. K. D. Mallikarjuna Rao, at saiskdmrao@iacs.res.in and mallik2arjun@gmail.com.

Benign Mid-Gap Halide Vacancy States in 2D-Bismuth-Based Halide Perovskite Microcrystals for Enhanced Broadband Photodetectors

Kuntal Singh[a#], Mozakkar Hossain[ab#], Pabitra Kumar Nayak[c], Sougata Karmakar[a], Akash Tripathi[d], Prakash Sarkar[a], Pratyasha Rudra[e], A. V. Muhammed Ali[a], G. Krishnamurthy Grandhi[f], Paola Vivo[f], Swastik Mondal[eg], K. V. Adarsh[d], Dibyajyoti Ghosh[ch], K. D. M. Rao[a]*

[a] *School of Applied & Interdisciplinary Sciences, Indian Association for the Cultivation of Science, Jadavpur, Kolkata 700032, India, E-mail: saiskdmrao@iacs.res.in (K. D. M. R.).*

[b]*Present Address: Department of Mechanical and Aerospace Engineering, University of California, Los Angeles, California 90095, USA*

[c]*Department of Chemistry, Indian Institute of Technology, Delhi, Hauz Khas, New Delhi 110016, India*

[d] *Department of Physics, Indian Institute of Science Education and Research, Bhopal, Madhya Pradesh 462066, India*

[e] *CSIR-Central Glass and Ceramic Research Institute, Kolkata 700032, India*

[f] *Hybrid Solar Cells, Faculty of Engineering and Natural Sciences, P.O. Box 541, FI-33014 Tampere University, Finland*

[g] *Academy of Scientific and Innovative Research (AcSIR), Ghaziabad 201002, India*

[h] *Department of Materials Science and Engineering, Indian Institute of Technology, Delhi, Hauz Khas, New Delhi 110016, India*

Abstract: Lead halide perovskites are widely recognized for their exceptional defect tolerance, setting the benchmark for high-performance optoelectronic applications. Conversely, low-toxicity perovskite-inspired materials (PIMs) typically exhibit suboptimal optoelectronic performance, primarily due to their intrinsic susceptibility to defects. In this study, we address this limitation by exploring the effects of halide vacancies in PIMs through the synthesis of non-stoichiometric $Cs_3Bi_2Br_3I_{5.2}$ microcrystals (MCs) with a trigonal crystal structure, incorporating iodine vacancies. Density Functional Theory simulations reveal that these iodine vacancies introduce benign mid-gap states that facilitate charge transport without perturbing band-edge excitons. As a result, the MCs exhibit sharp photoluminescence emission with a linewidth of 140 meV and a minimal Stokes shift of 147 meV, indicative of efficient band-edge recombination. Transient absorption measurements confirm photo induced mid-gap absorption. While Space charge limited current measurements demonstrate low trap densities of 1.1×10^{11} cm^{-3}, despite the presence of iodine vacancies. We further fabricated self-driven broadband photodetectors using 2D-$Cs_3Bi_2Br_3I_{5.2}$ MCs, achieving a high responsivity of 0.9 A/W with a photoresponse extending to 800 nm. While ultrafast carrier localization remains a performance-limiting factor, the room-temperature carrier mobility exceeds 1 $cm^2V^{-1}s^{-1}$, positioning Cs-Bi-Br-I as a highly promising low-toxicity absorber for advanced optoelectronic and light-harvesting applications.

Introduction:

Defect chemistry, precisely the nature and concentration of defects, plays a crucial role in advancing cost-effective, solution-processed semiconductors for high-performance optoelectronic devices. Lead halide perovskites (LHPs), distinguished by their ns^2 electronic configuration, exhibit exceptional defect tolerance, primarily due to the antibonding interactions between Pb 6*s* orbitals and halide *p* orbitals.[1–3] This intrinsic tolerance has enabled LHPs to achieve power

conversion efficiencies exceeding 26% in solar cells[4] and exhibit excellent light-emitting properties,[5] establishing them as leading materials in optoelectronics. However, as the halide composition transitions from iodide to bromide and chloride, increasing ionicity and reduced dielectric screening lead to diminished defect tolerance.[6,7] Despite the existence of deep defect levels, the strong polarizability of Pb^{2+} facilitates efficient dielectric screening, thereby preserving the superior optoelectronic performance of LHPs. In contrast, bismuth(III) halide perovskite-inspired materials (Bi-PIMs) provide environmentally sustainable alternatives yet often demonstrate lower performance relative to LHPs.[8–10] The heavier Bi^{3+} cation provides a high dielectric constant, but its deeper *s* orbitals have minimal impact on the valence band edge, resulting in suboptimal photovoltaic efficiency.[8,11,12] Moreover, strong carrier-phonon coupling and self-trapping effects in Bi-PIMs frequently induce non-radiative recombination, further diminishing device performance.[13,14] These intrinsic limitations, particularly concerning defect tolerance, band alignment, and charge carrier mobility, have hindered Bi-PIMs from reaching the high efficiencies characteristic of LHPs despite their eco-friendly composition

Halide vacancies, particularly iodine and bromine, are commonly observed in Bi-PIMs due to their polar nature and low formation energy (0.1 to 0.6 eV).[15] These vacancies can introduce deep mid-gap states that trap charge carriers, leading to increased non-radiative recombination, which severely compromises device efficiency.[16,17] Interestingly, theoretical models of lead halide perovskites suggest that iodine vacancies may not induce significant non-radiative recombination, implying a potential for defect tolerance.[18] However, the experimental control and precise quantification of these vacancies, particularly in thin films, remain challenging due to the presence of grain boundaries and interface effects.[19,20] Bulk single crystals provide a more controlled environment for vacancy analysis, although their considerable thickness may hinder efficient

charge extraction.[21] Microcrystals (MCs), with their higher surface-to-volume ratios and enhanced charge diffusion lengths, represent an optimal framework for investigating and mitigating the adverse effects of halide vacancies. Additionally, facet-oriented growth in microcrystals enhances charge transport, making them ideal for studying defect dynamics and improving material performance.[21]

For example, BiOI exhibits shallow iodine vacancy states, suggesting defect tolerance; however, strong electron-phonon coupling in these materials restricts carrier lifetimes to less than 5 ns.[22] Similarly, $Cs_2AgBiBr_6$ exhibits ultrafast carrier localization due to self-trapping, leading to shortened diffusion lengths and complicating the verification of defect tolerance.[23–25] Conversely, bromine vacancies in $Cs_2AgTlBr_6$ and $Cs_2AgBiBr_6$ have been shown to significantly enhance electrical conductivity through n-type doping, attributed to bromine degassing.[26] Additionally, Zheng *et al.* further demonstrated that Br^- vacancies in $Cs_3Bi_2Br_9$ induce impurity phase formation, whereas Ag^+ cations effectively passivate these vacancies, improving structural stability.[27] Despite these advancements, most studies are based on computational models,[11] suggesting that defect tolerance may be achievable, though experimental control remains a significant challenge. Comprehensive experimental studies are required to elucidate the complex relationships between defects and optoelectronic performance in Bi-PIMs. Furthermore, increasing the antimony content in mixed Sb-Bi halide elpasolites ($Cs_2Ag(Sb_xBi_{1-x})Br_6$) reduces defect tolerance by introducing sub-bandgap or mid-gap states, which generate strain, energy disorder, and lower photovoltaic efficiency.[28] While sub-bandgap defect states have also been observed in Cu_2AgBiI_6, their influence on Bi-PIM performance remains largely unexplored.[29] In lead halide perovskites, these defect states are often attributed to point defects,[7] and in some cases, they can enhance photodetection by extending the photosensitivity beyond the material's intrinsic bandgap.[30]

Understanding the intricate interplay between defects and optoelectronic properties in Bi-PIMs is essential for identifying materials with enhanced defect tolerance. Halide mixing with vacancy-ordered $Cs_3Bi_2I_9$, with its two-dimensional structure and improved charge transport, emerges as a promising Bi-PIM.[31,32] Defect calculations under iodine-deficient, bismuth-rich conditions reveal that iodine vacancies dominate, forming deep donor levels near the conduction band minimum, suggesting a low carrier capture cross-section[1,33] and emphasizing the importance of defect engineering to optimize device performance.

This study examines the influence of halide vacancies on the optoelectronic properties of Bi-PIMs, an area that remains underexplored due to the complexity of experimentally controlling and quantifying these vacancies. We utilize an Ag-assisted synthesis method to fabricate two-dimensional $Cs_3Bi_2Br_3I_{5.2}$ microcrystals (MCs) with intentionally engineered iodine vacancies. Through a modified hot-spin casting technique, we achieve facet-oriented growth of the MCs, which plays a pivotal role in enhancing their optoelectronic behavior. Comprehensive structural and electronic characterizations are conducted via single-crystal X-ray diffraction (SC-XRD), charge density mapping, and Density Functional Theory (DFT) simulations. Additionally, the photoluminescence (PL) properties, exciton binding energy, and electron-phonon coupling are evaluated, offering deep insights into their potential for self-powered broadband photodetector applications. The intentional iodine vacancy creation modifies the electronic structure, inducing mid-gap states, confirmed by transient absorption spectroscopy (TAS), that facilitate charge transport without triggering adverse recombination processes. Our results unfold the potential of iodine vacancies as a tool for precise modulation of the spectral response, leading to significant enhancements in the optoelectronic performance of Bi-PIMs.

Results and discussion:

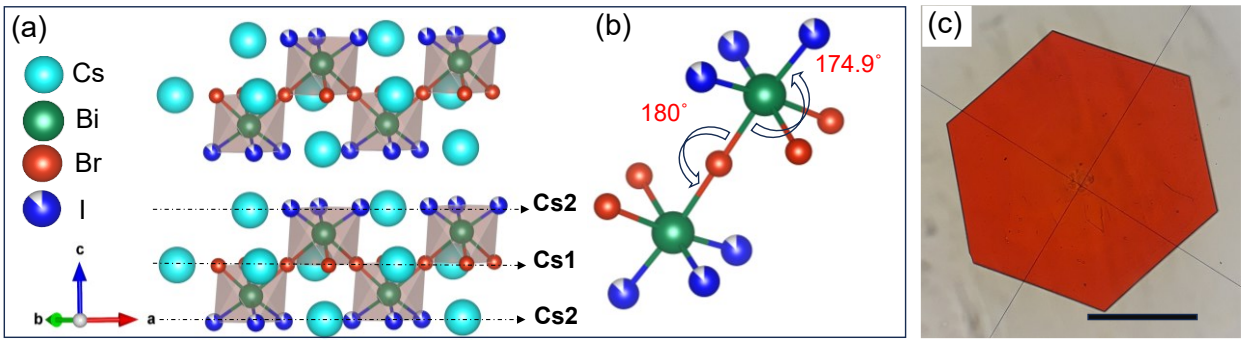

Figure 1: Crystallographic characterization of 2D $Cs_3Bi_2Br_3I_{5.2}$ Single Crystals from single crystal X-ray diffraction (SCXRD): (a) Unit cell representation of the crystal structure considering The crystal structure on a large scale, illustrating the arrangement of atoms within the crystal lattice. Blue and gray within the identical spheres represent iodine atoms, with gray indicating vacancies. (b) A magnified view focusing on a connected octahedron, highlighting the Br-I-Br bond angle. (c) An optical microscopy image showcasing a single microcrystal with a well-defined hexagonal morphology. (scale bar 50 μm).

Facet-oriented 2D-$Cs_3Bi_2Br_3I_{5.2}$ microcrystals (MCs) are synthesized using a modified hot-spin casting method. Initially, a precursor solution is prepared by dissolving the raw materials as CsI, $BiBr_3$, and BiI_3 with a stoichiometric ratio (3:1:1) in addition to AgI in dimethyl sulfoxide (DMSO) solvent at 70°C for 16 hours. UV-ozone-treated glass substrates are pre-heated at 150°C for 8 minutes, then spin-coated with the precursor solution. Heat transfer during spin coating generates heterogeneous nucleation centers,[34] facilitating crystal growth (**see Figure S1** and **Experimental section**). Substrates undergo vacuum drying for 24 hours, promoting nucleation center growth and forming facet-oriented 2D-$Cs_3Bi_2Br_3I_{5.2}$ MCs. Vacuum drying is crucial for perovskite MC formation and impurity phase mitigation. Slow solvent evaporation prolongs nuclei center growth, yielding MCs with iodine vacancies by eliminating neutral iodine molecules through I_2 degassing.[26] The addition of silver ions provides structural stability by passivation of I^- vacancies.[27] The method presents precise control over crystal size and facet orientation, ensuring impurity-free 2D-$Cs_3Bi_2Br_3I_{5.2}$ synthesis.

Table 1: The crystal structure refinement of parameters of 2D-$Cs_3Bi_2Br_3I_{5.2}$ MC from SCXRD and comparison with $Cs_3Bi_2Br_3I_6$.[31]

Empirical formula	**$Cs_3Bi_2Br_3I_6$**	**$Cs_3Bi_2Br_3I_{5.2}$**
Crystal system	Trigonal	Trigonal
Space group	P-3m1	P-3m1
a/Å	8.3605(5)	8.2207(12)
b/Å	8.3605(5)	8.2207(12)
c/Å	10.2747(5)	10.104(2)
α/°	90	90
β/°	90	90
γ/°	120	120
Volume/Å^3	621.97	591.3(2)
Octahedral Volume/Å^3	-	33.5601
Z	1	1
Density (calculated) g/cm^3	4.853	4.827
Absorption coefficient (μ)/mm^{-1}	-	31.266

The structural characterization of 2D-$Cs_3Bi_2Br_3I_{5.2}$ MCs was performed using single-crystal X-ray diffraction (SC-XRD). The crystal structure was determined, revealing a trigonal lattice with space group P-3m1 and lattice parameters a = b = 8.2207(12) Å, c = 10.104(2) Å, α = β = 90°, γ = 120°, Z = 1, and volume = 591.3(2) Å^3 (see **Figure 1a, Table 1** and **Table S1**). In **Table S2-S5**, the lattice parameters are meticulously detailed. The 2D-$Cs_3Bi_2Br_3I_{5.2}$ unit cell exhibits a smaller volume (ΔV = 30 Å^3) compared to the reported $Cs_3Bi_2Br_3I_6$ crystal lattice, attributed to iodine vacancies.[31] Within the crystal lattice, Cs1 and Cs2 designate distinct Cs atoms. Cs1, located at Wyckoff site 1b, segregates neighbouring octahedra, while Cs2, situated at Wyckoff site 2d, occupies the octahedral voids (see **Figure 1a**). The corner-sharing of two $[BiX_6]^{3-}$ octahedra via Br atoms results in a Bi-Br bond length (3.0079(4) Å) slightly greater than the Bi-I bond length (2.8590(6) Å), reflecting the smaller ionic radius of Br (1.96 Å) compared to I (2.06 Å). Additionally, the Bi-Br-Bi and I-Bi-Br bond angles of 2D-$Cs_3Bi_2Br_3I_{5.2}$ are found to be 180(0)°

and 174.9(19)°, respectively (see **Figure 1b**), indicating strong orbital overlap that reduces the effective carrier mass and enhances carrier mobility across inter-octahedral connections.[35] However, the reduced bond angle in intra-octahedral connections, attributed to iodine vacancies, leads to charge localization near the uncoordinated Bi atom (vide infra).

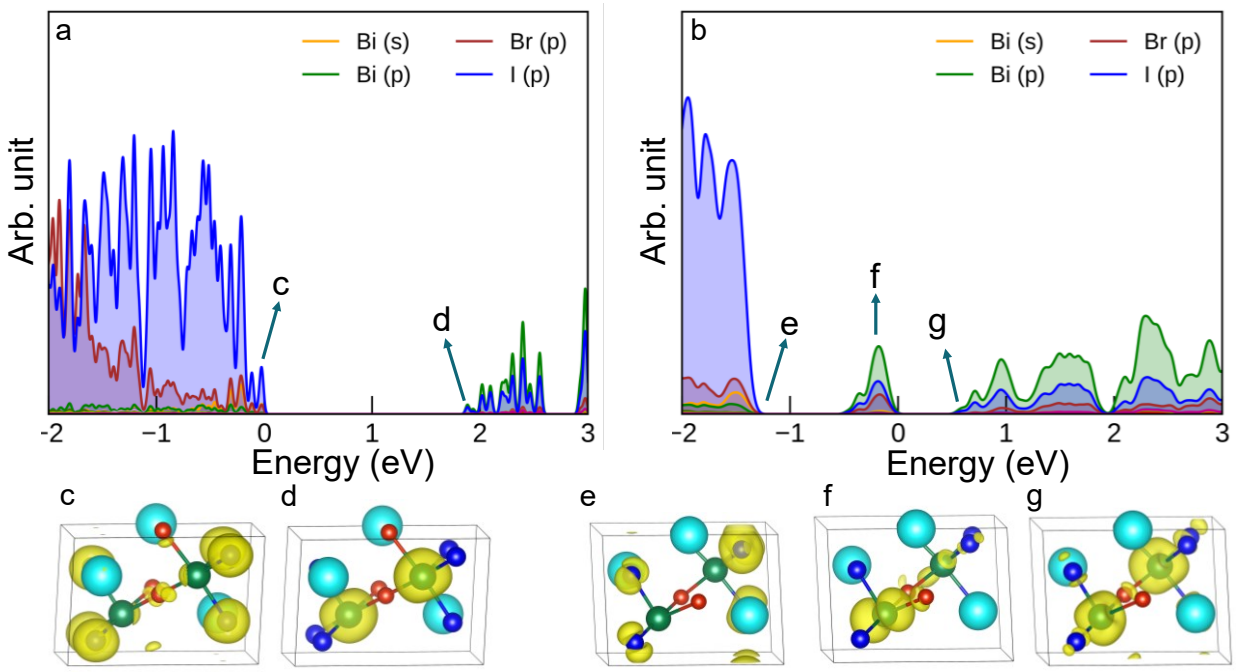

Figure 2: The element-projected Density of States (DOS) results for optimized geometry of (a) pristine $Cs_3Bi_2Br_3I_6$ and (b) $Cs_3Bi_2Br_3I_5$. Alphabets within the DOS plots correspond to charge density plots labelled below as (c-g). Charge density plots illustrate (c) VBM and (d) CBM states of pristine $Cs_3Bi_2Br_3I_6$. Similarly, (e), (f), and (g) represent VBM, mid-gap Bi-states, and CBM, respectively. Calculations are performed using the hybrid HSE06 functional with spin-orbit coupling. The Fermi energy of $Cs_3Bi_2Br_3I_6$ and $Cs_3Bi_2Br_3I_5$ materials are scaled to 0 eV. Key: Cyan: Cs, Olive: Bi, Red: Br, Blue: I; Yellow-colored iso-surface represents the spatial distribution of electron density.

Powder X-ray diffraction (XRD) analysis verifies the facet-oriented nature of 2D-$Cs_3Bi_2Br_3I_{5.2}$ crystals along the {001} plane (see **Figure S2a**), aligning with simulated XRD patterns. Moreover, time-dependent XRD data presented in **Figure S3** illustrates the enduring stability of 2D-$Cs_3Bi_2Br_3I_{5.2}$ MCs, exhibiting no impurity peaks even after prolonged environmental exposure. Transmission electron microscopy (TEM) further validates the crystal structure of 2D-$Cs_3Bi_2Br_3I_{5.2}$ microcrystals (MCs). The selected area electron diffraction (SAED)

patterns (**see Figure S2b**) reveal distinct and intense spots corresponding to the (003) and (006) planes, confirming the crystalline structure.

To elucidate the atomistic characteristics of 2D-$Cs_3Bi_2Br_3I_{5.2}$, we conducted highly accurate Density Functional Theory-based (DFT) simulations (see **computational methodology** section in SI). For computational modelling of the $Cs_3Bi_2Br_3I_{5.2}$ surface, we initially utilized the pristine $Cs_3Bi_2Br_3I_6$ structure, introducing an I-vacancy within the pristine unit cell to obtain $Cs_3Bi_2Br_3I_5$ (see **Figure S4-S5**). The structural integrity of the I-vacancy configuration was confirmed through geometric optimization at the electronic ground state. The partial density of states (pDOS) plot in **Figure 2a-b and S6** illustrates that pristine $Cs_3Bi_2Br_3I_6$ lacks defect-induced trap states within the band gap. The calculated indirect band gap, employing computationally intensive HSE06 exchange-correlation functionals with consideration for spin-orbit coupling (**Figure 2a**), is determined to be 1.90 eV (with a direct gap of 1.99 eV). Examination of pDOS and charge densities at the band edge states elucidates that the VBM state primarily originates from the 4p(5p) orbitals of Br(I), while the CBM state is predominantly composed of the 6p orbitals of Bi, along with the 4p(5p) orbitals of Br(I).

To model realistic $Cs_3Bi_2Br_3I_{5.2}$, we introduce an iodine vacancy (V_I) along the edge of the layered structure, resulting in $Cs_3Bi_2Br_3I_5$ (**Figure S4a**).[36] The vacancy formation energy is calculated at 1.59 eV per formula unit, comparable to halide vacancy formation energy in $MAPbI_3$.[36–38] The optimized geometry depicts that Bismuth (Bi), situated adjacent to the iodine defect, forms bonds with two iodines (excluding one dangling bond) and three bromines (b), sharing octahedra with nearby Bi in a Fac-Mer fashion. After introducing the iodine vacancy, no significant distortions in the intra-octahedral Bi-I or Bi-Br bond lengths, nor changes in the Br-Bi-

Br/I-Bi-I bond angles, are observed. However, the inter-octahedral Bi-Br-Bi angle shifts significantly from 180.6° to 160.6°,

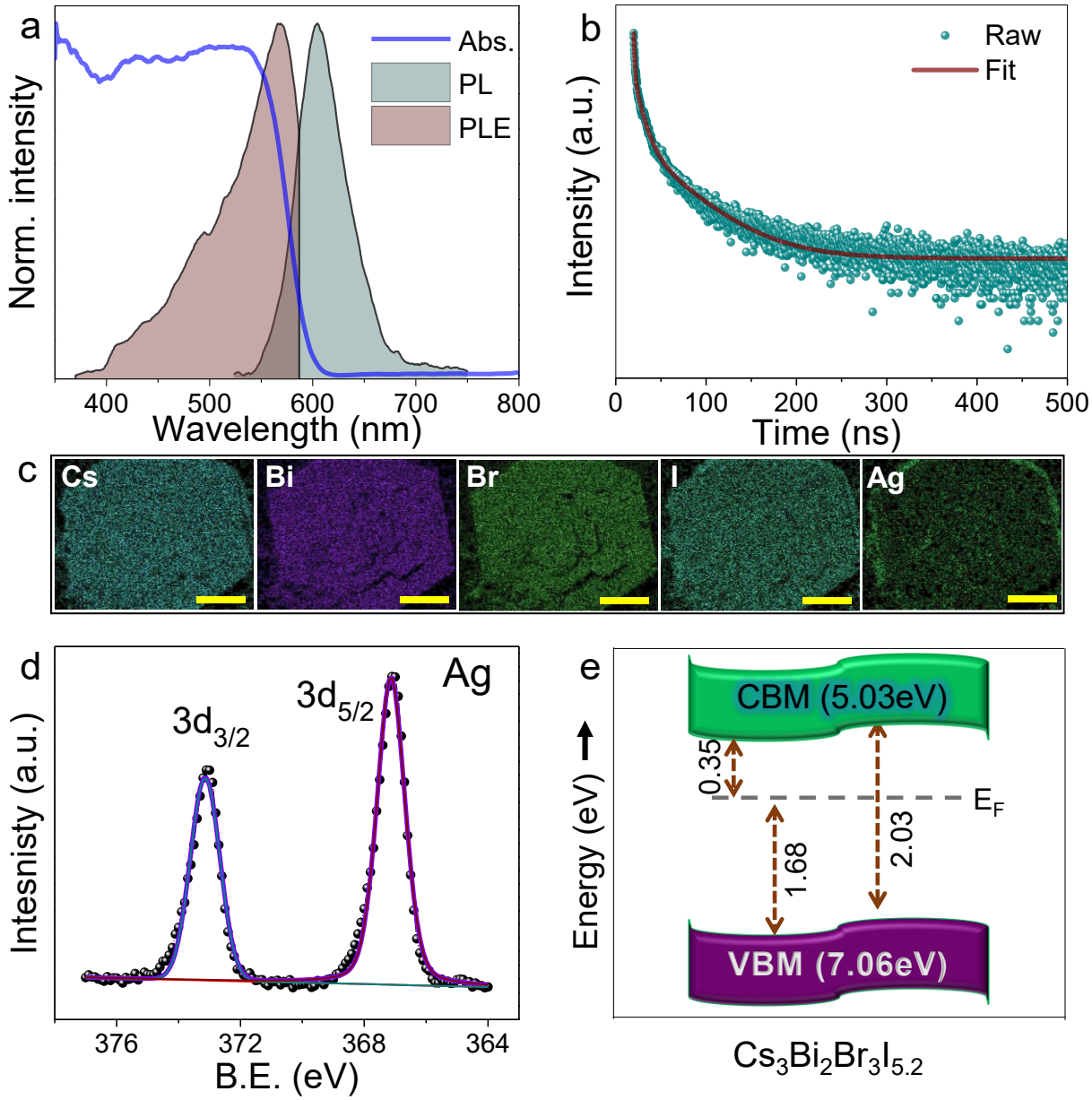

Figure 3. Optical and morphological characterization of 2D $Cs_3Bi_2Br_3I_{5.2}$ MCs. (a) UV-visible absorption spectra, steady-state PL spectra, and corresponding PLE spectra of 2D $Cs_3Bi_2Br_3I_{5.2}$ MCs. (b) Time-resolved PL decay of $Cs_3Bi_2Br_3I_{5.2}$ MCs, (c) Elemental mapping (EDX) of $Cs_3Bi_2Br_3I_{5.2}$ MCs (scale bar 50 µm), (d) core level X-ray photoelectron spectra (XPS) of Ag 3d element in $Cs_3Bi_2Br_3I_{5.2}$ MCs, (e) electronic band diagram of $Cs_3Bi_2Br_3I_{5.2}$ MCs, estimated through ultraviolet photoelectron spectroscopy (UPS).

indicating inter-octahedral tilting due to the iodine vacancy. Thus, the iodine vacancy causes minor distortions in local geometry due to the uncoordinated Bi. The Bi-I bond opposite the dangling bond elongates by 0.13 Å from the pristine structure during structural relaxation after introducing V_I. Perturbations in nearby bond lengths and angles are detailed in **Tables S6** and **S7** in the supporting information. The absence of major structural modifications with iodine vacancy also suggests the preserved structural stability of $Cs_3Bi_2Br_3I_5$, which matches our experimental observations well. The calculated indirect bandgap for $Cs_3Bi_2Br_3I_5$ is 1.90 eV, with Bi-states emerging as mid-gap states, 0.61 eV below the CBM (**Figure 2b** and **Figure S6-S7**). The band structure plot (**Figure S6**) confirms the indirect nature of the bandgap for both pristine and I-vacancy materials. The orbital contributions of the VBM and CBM states for $Cs_3Bi_2Br_3I_5$ are similar to the pristine counterpart. **Figures 2c-2f** display charge density plots for pristine $Cs_3Bi_2Br_3I_6$ and $Cs_3Bi_2Br_3I_5$ with iodine vacancy. In $Cs_3Bi_2Br_3I_6$ (**Figures 2c-2d**), the charge is delocalized at the band edges with no significant defect states. In contrast, $Cs_3Bi_2Br_3I_5$ (**Figure 2f**) with an iodine vacancy shows highly localized Bi-states, attributed to an uncoordinated electropositive Bi atom. Further, we employ *ab initio* molecular dynamics simulation to explore the thermal stability of pristine and vacancy-dominated materials at 300 K (see **computational methodology** in SI for details). The potential energy, temperature, and root mean square fluctuations (RMSFs) in **Video S1-S2**, **Figure S8-S11** and **Section S1** depict the structural stability of pristine $Cs_3Bi_2Br_3I_6$ and $Cs_3Bi_2Br_3I_5$.

Figure 3a presents the UV-visible absorption, photoluminescence (PL), and photoluminescence excitation (PLE) spectra of $Cs_3Bi_2Br_3I_{5.2}$ MCs. Notably, the absorption spectra lack the excitonic peak at 490 nm present in 0D-$Cs_3Bi_2I_9$, suggesting enhanced band edge absorption and improved optoelectronic performance.[39] The indirect and direct bandgaps of

$Cs_3Bi_2Br_3I_{5.2}$ MCs are estimated to be 2.03 eV and 2.12 eV, respectively, indicating a quasi-direct band transition (**Figure S12 and Section S2**). This bandgap closely matches those of 0D-$Cs_3Bi_2I_9$ and 2D-$Cs_3Bi_2Br_3I_{5.2}$, prompting further examination of the electronic structure and optoelectronic properties.[31,40] However-due to the low (~10%) fill factor of the large microcrystals (20–300 μm in size) on the substrate and low density mid gap states, as shown in the inset of **Figure S13a**, it is challenging to distinguish mid-gap absorption characteristics from scattering effects below the band edge energy.

The photoluminescence (PL) spectrum of 2D-$Cs_3Bi_2Br_3I_{5.2}$ MCs reveals a sharp emission peak at 605 nm, with a linewidth of 140 meV, closely matching the absorption edge and photoluminescence excitation (PLE) spectra (see **Figure 3a**). This suggests that the emission predominantly arises from band-edge recombination, with a minimal Stokes shift of 147 meV, which is significantly lower than those observed in $Cs_3Bi_2Br_9$ (237 meV) and $Cs_3Sb_2I_9$ (520 meV).[41,42] Notably, no strong broad defect-related or self-trapped exciton (STE) emission, typically observed in Bi-PIMs, was detected.[43] This is likely due to the suppression caused by the dominant and narrow band-edge recombination. However, the PL spectrum shows an asymmetry skewed towards lower energies (see **Figure S13b**), with a closer look at 1.7–1.9 eV revealing a slight but noticeable PL emission instead of a sharp decay. This extended PL can be attributed to trap-state recombination, which is consistent with other metal halide perovskites.[30,44,45] Choi *et al*. observed similar low-intensity PL peaks below the band edge in 2D-BA_2PbBr_4 single crystals due to trap-assisted recombination,[30] while mid-gap state photodetection studies in perovskites confirm low-energy PL emissions from trap states.[30,45] In the case of $Cs_3Bi_2Br_3I_{5.2}$ MCs, the intensity of the defect-related PL peak is only about 6% of the band-edge PL peak intensity. This suggests

minimal trap-assisted recombination and indicates that carrier's recombination mainly occurs between the band-edges, highlighting the benign nature of the mid-gap states.

Figure 3b illustrates the time-resolved PL (TRPL) decay curve of 2D-$Cs_3Bi_2Br_3I_{5.2}$ MCs, fitted with a tri-exponential decay function, yielding fast decay lifetimes of 1 and 8 ns alongside a slow decay component of 49 ns. The prolonged slow decay component, exceeding 10 ns, highlights the suitability of the 2D-$Cs_3Bi_2Br_3I_{5.2}$ for efficient charge separation in device applications, such as photodetectors and solar cells.[11,46] Moreover, 2D-$Cs_3Bi_2Br_3I_{5.2}$ MCs exhibit a high tolerance to elevated temperatures up to 430°C, consistent with the properties of $Cs_3Bi_2Br_3I_6$, making them viable for practical applications (see **Figure S14**).[31] Energy Dispersive X-ray (EDX) mapping of 2D-$Cs_3Bi_2Br_3I_{5.2}$ confirms the homogeneous distribution of Cs, Bi, Br, I, and Ag across the MC surface (**Figure 3c**). This observation is supported by X-ray photoelectron spectroscopy (XPS) survey and core-level spectra (**Figure 3d** and **Figures S15-S16**), which confirm the presence and valence states of Cs^+, Bi^{3+}, Br^-, I^-, and Ag^+. The elemental ratio (Cs:Bi:Br:I = 2.3:2:3:5.3) closely aligns with the experimental stoichiometry (**Table S8**). Halide vacancies, particularly iodine vacancies, influence charge transport in low-dimensional halide perovskites. [26,47] To address iodine deficiency in 2D-$Cs_3Bi_2Br_3I_{5.2}$, Ag^+ cations were introduced via AgI. EDX and XPS confirm Ag^+ at vacancy sites (**Figures 3c, 3d**), though single-crystal XRD showed no Ag in the lattice, indicating possible interstitial or surface incorporation. Zhang *et al.* reported AgBr passivates bromine vacancies in $Cs_3Bi_2Br_9$, preventing oxidation.[27] Anupam et al. found Ag at interstitial sites in $Cs_3Bi_2Br_9$, inducing bound excitons.[43] Similarly, AgI in 2D-$Cs_3Bi_2Br_3I_{5.2}$ likely stabilizes the structure, mitigating iodine vacancy effects and enhancing material stability.

Ultraviolet photoelectron spectroscopy (UPS) analysis of 2D-$Cs_3Bi_2Br_3I_{5.2}$ reveals a Fermi level at -5.38 eV, determined from the UPS cut-off region, with the valence band maximum (VBM)

extracted the UPS tail onset (**Figure S17**). The conduction band minimum (CBM) is estimated by adding the bandgap from the Tauc plot to the VBM (**Figure S17c**). The band diagram of 2D-$Cs_3Bi_2Br_3I_{5.2}$ (**Figure 3e**, **Table S9**) confirms its n-type semiconducting behaviour, consistent with the DFT-calculated pDOS plot (**Figure 2b**), which shows a donor level below the CBM. The n-type characteristics of $Cs_3Bi_2Br_3I_{5.2}$ MCs stem from iodine vacancies (V_I), which introduce additional electrons. This aligns with prior studies where iodine degassing induced n-type doping in Cs_2SnI_6[47] and bromine vacancies enhanced n-type doping in $Cs_2AgTlBr_6$.[26] Similarly, donor levels ~0.52 eV and ~0.40 eV below the CBM were observed in iodine-deficient Cs_2SnI_6,[48] and $(MA)_2Pb(SCN)_2I_2$,[49] respectively. Moreover, our theoretical calculations on $Cs_3Bi_2Br_3I_{5.2}$ reveal that iodine vacancies increase electron density near bismuth atoms, tilting the Bi–Br–Bi bond angle from 180.6° to 160.6°. These electron-rich bismuth states create mid-gap states ~0.61 eV below the CBM, as confirmed by UPS), which places them below the Fermi level (0.35 eV from the CBM). Combined UPS analysis and analyses confirm that iodine vacancy-induced mid-gap states are the primary source of n-type behaviour.

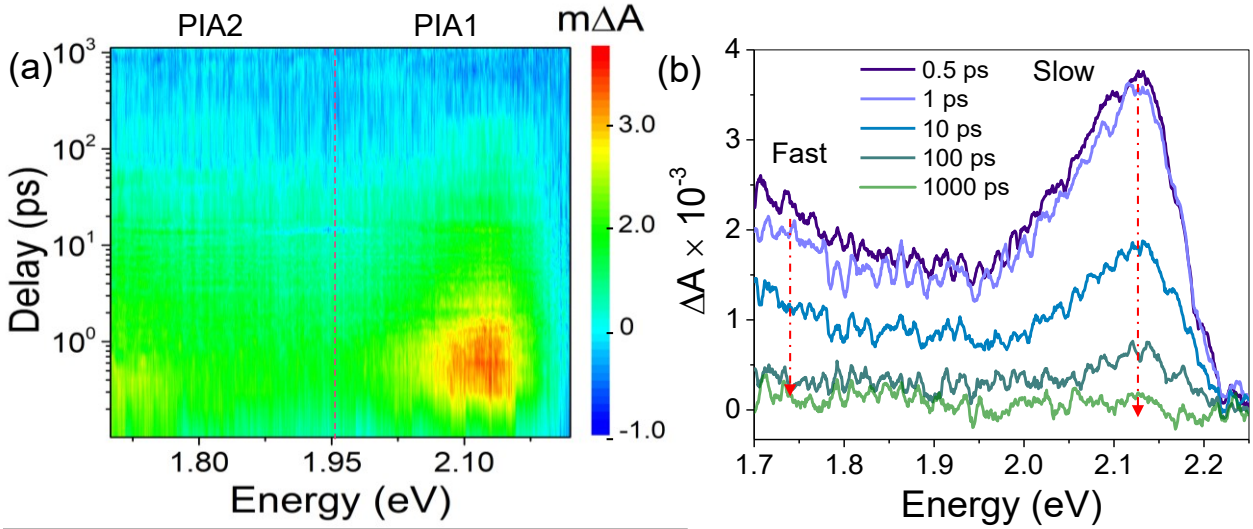

Figure 4. (a) Contour plot of the room temperature transient absorption (TA) spectra of $Cs_3Bi_2Br_3I_{5.2}$ under 400 nm pump at a fluence of 1000 μJ/cm². (b) Cross section of the contour plots at selected pump-probe delay times, highlighting the band-edge and mid-gap states at two different probe energies.

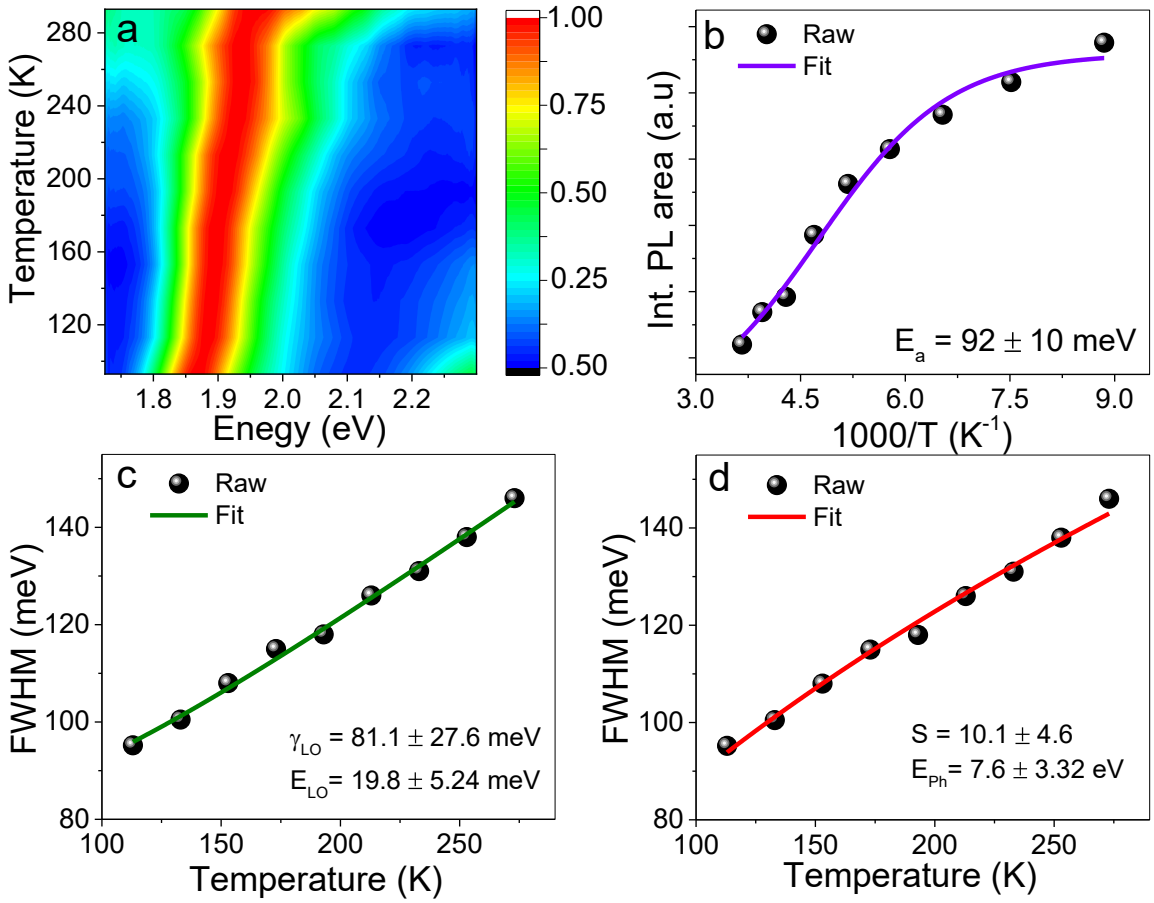

Figure 5. Temperature-dependent Photoluminescence spectra of 2D $Cs_3Bi_2Br_3I_{5.2}$ MCs. (a) Changes in PL spectra with varying temperature ranges from 93 K to 273 K. (d) Integrated PL area vs 1/T plot for the estimation of exciton binding energy (χ^2 = 0.987). (c) Least square fitting of full-width half maxima (FWHM) *vs*. temperature using Rudin's model (green line) to estimate effective phonon contribution (χ^2 = 0.994) and (d) Toyozaya model (red line) to calculate the Huang−Rhys electron-phonon coupling parameter (*S*) and associated phonon energy (χ^2 = 0.990). Here, the symbols and solid lines resemble the raw and fitted data, respectively.

The ultrafast transient absorption spectroscopy (TAS) was studied using an above-bandgap 3.1 eV pump pulse with a fluence of 1000 μJ/cm², while the probe energy was varied from 1.7 to 2.25 eV to explore sub-bandgap absorption dynamics. The contour plot of the TA data and the slices of the spectrum at different pump-probe time delays (**Figure 4a-4b**) reveal two distinct photoinduced absorption features. The first feature, a photoinduced absorption peak (PIA1), is centered at 2.1 eV with a full width at half maximum (FWHM) of approximately 160 meV in the

bandgap region, resembling band-edge absorption commonly observed in perovskite materials.[23,50] The second feature is a broad sub-bandgap absorption (PIA2) spanning 1.7–1.95 eV.

The asymmetric nature of PIA1 is attributed to the combined effects of mid-gap states. As shown in **Figure 4b**, PIA1 exhibits a significantly slower decay compared to PIA2, likely due to hot carrier decay dynamics and polaron formation, which localizes excitons through electron-phonon coupling via the deformation potential.[23,51,52] Similar behavior has been observed in several low-dimensional Bi-based perovskites.[23,51,52] In contrast, PIA2 demonstrates a faster decay, indicating distinct decay mechanisms. The differing decay dynamics of PIA1 and PIA2 confirm their distinct origins and contributions to transient absorbance at different energy regions.

For a better understanding of thermal quenching behavior in 2D-$Cs_3Bi_2Br_3I_{5.2}$ MCs, temperature-dependent steady-state PL has been studied, as depicted in **Figure 5a**. A gradual decrease in PL intensity is observed with increasing temperature. This behavior can be explained by PL quenching due to thermal energy, which enhances non-radiative recombination at higher temperatures.[53–55] The exciton binding energy is determined by fitting the integrated PL area plot against temperature (**Figure 5b**) using the Arrhenius equation 1.[53,54]

$$I(T) = \frac{I_0}{\left[1 + A\exp\left(-\frac{E_b}{k_B T}\right)\right]} \quad (1)$$

Where *I(T)* is the integrated PL area at temperature *T*, *I(0)* is the int PL area at temperature 0K, E_b is the exciton binding energy, and k_B is the Boltzmann's constant. The exciton binding energy for 2D-$Cs_3Bi_2Br_3I_{5.2}$ MCs is estimated to be 92 meV, which is lower than that of other halide perovskites such as $Rb_3Sb_2I_9$, $K_3Sb_2I_9$, $Cs_3Sb_2I_9$, $Cs_3Bi_2I_9$, and $MA_3Bi_2I_9$.[54,56,57]Lower excitonic binding energy contributes to improved charge carrier generation and extraction in optoelectronic devices.[53,58]

The temperature-dependent PL linewidth is fitted with Rudin's model (**Figure 5c**) to determine the effective phonon interactions. The equation can be written as,

$$\Gamma(T) = \Gamma_0 + \Gamma_{ac} + \Gamma_{LO}$$

$$= \Gamma_0 + \Upsilon_{ac}T + \frac{\Upsilon_{LO}}{\exp\left(\frac{E_{LO}}{k_B T}-1\right)} \text{ …….. (2)}$$

Where $\Gamma(T)$ represents the total linewidth broadening at T temperature, Γ_0 the temperature-independent broadening due to lattice disorder.[59,60] Γ_{ac} and Γ_{LO} denote the broadening contributions from electron coupling with acoustic phonons and Fröhlich scattering of LO phonons, while γ_{LO} and γ_{ac} are corresponding coupling constants, respectively. The estimated LO phonon energy (E_{LO}) is found to be 19.8 ± 5.2 meV (159.67 cm^{-1}), well aligns well with the strongest Raman mode A_{1g} (see **Figure S18** and **Table S10**). The corresponding LO phonon coupling constant γ_{LO} is 81.1 ± 27.6 meV, significantly lower than in other halide perovskites. This suggests reduced self-trapped exciton (STE) formation, leading to enhanced charge carrier transport.[39,59]

Furthermore, the Huang−Rhys (S) parameter, quantifying electron-phonon coupling strength due to distortion, is estimated for 2D-$Cs_3Bi_2Br_3I_{5.2}$ MCs using the temperature-dependent FWHM plot (**Figure 5d**) by fitting to the Toyazowa model with the equation 2. [39,55,59]

$$w(T) = 2.36\sqrt{S}E_{Ph}[\coth(\frac{E_{Ph}}{2k_B T})]^{1/2} \text{ ---------- (2)}$$

Where $w(T)$ represents the FWHM at temperature T, and E_{Ph} is the phonon energy. The Huang−Rhys (S) parameter and the associated phonon energy for 2D-$Cs_3Bi_2Br_3I_{5.2}$ MCs are estimated to be 10 ± 1.7 and 7.6 ± 1.2 meV, respectively. Notably, the phonon energy closely aligns the Raman scattering peak at 57.7 cm^{-1} of 2D-$Cs_3Bi_2Br_3I_{5.2}$ MCs (**Figure S18** and **Table S10**), originating from the Bi-I bending mode. The coupling parameter S is lower than those observed in 2D-$Rb_3Sb_2I_9$ (21.2), 2D-$Cs_3Sb_2I_9$ (42.7), 2D-$Cs_3Bi_2I_6Cl_3$ (212), and 0D-$Cs_3Bi_2I_9$

(79.5).[39,55] The lower γ_{LO} *and S*-value are attributed to the formation of the layered structure, which allows for greater distortion tolerance compared to 0D halide perovskites.[55] Additionally, the quasi-direct bandgap nature reduces phonon interaction, resulting in lower electron-phonon coupling in 2D-$Cs_3Bi_2Br_3I_{5.2}$ MCs, even with mid-gap states arising from iodine vacancies.

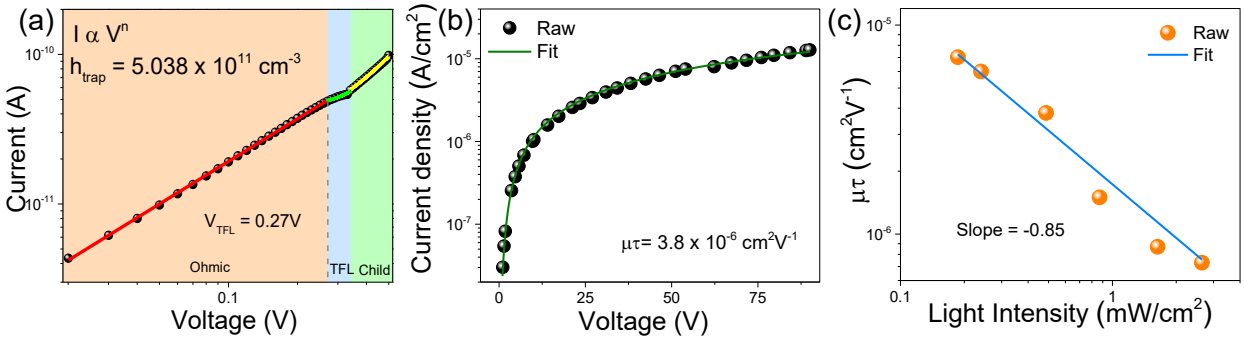

Figure 6: (a) Space Charge Limited Current (SCLC) model fitting of dark current-voltage curves for 2D-$Cs_3Bi_2Br_3I_{5.2}$ MCs. (b) Voltage-dependent photocurrent density plot for 2D-$Cs_3Bi_2Br_3I_{5.2}$ MCs, fitted with Hecht's equation. Solid spheres show experimental data, and colored curves represent the fitted model. (c) Power-law fitting of mobility-lifetime product versus light intensity.

The electronic properties of 2D-$Cs_3Bi_2Br_3I_{5.2}$ MCs are analysed using space charge limited current (SCLC) analysis in the dark (**Figure 6a**). The SCLC analysis identified three regimes characterized by the power factor (n) in the equation $I \alpha V^n$.[61,62] In the first regime (light orange), the current increases linearly, indicating the ohmic region ($n = 1$). The second regime (light grey) represents the trap-filled limited region ($n > 3$), where injected carriers fill trap states. The transition voltage from the ohmic to the trap-filled region is defined as the trap-filled limited voltage (V_{TFL}), and the trap density (η_{trap}) is calculated using equation 3 (**Section S3**).[61–63]

$$\eta_{trap} = \frac{2\varepsilon_0 \varepsilon V_{TFL}}{qL^2} \quad \text{(3)}$$

where ε_0, ε, q, and L are free space permittivity, relative dielectric constant, elementary charge, and MC length, respectively. The V_{TFL} value for 2D-$Cs_3Bi_2Br_3I_{5.2}$ MC is 0.27 V (**Figure 6a**), with a corresponding trap density (η) is ~1.1 × 10^{11} cm^{-3}. This trap density is five orders of magnitude lower than that of reported perovskite thin films but slightly higher than in single

crystals, likely due to iodine vacancy defects.[64,65] In the third regime (light green), the current follows the Mott-Gurney law(n = 2, Child's regime), enabling the calculation of carrier mobility (μ), which is found to be 1.12 $cm^2V^{-1}S^{-1}$ (**Section S3**).[63,66]

The current-voltage characteristic under light illumination of 2D-$Cs_3Bi_2Br_3I_{5.2}$ MC is evaluated using the modified Hecht equation to extract the $\mu\tau$ product (**Figure 6a**, details in **Section S4**).[31,64] The estimated $\mu\tau$ product is 3.8×10^{-6} $cm^{-2}V^{-1}$, comparable to other 2D halide perovskites.[26] Additionally, the diffusion length (L_D) of MC is estimated to be 3.08 µm (details in **Section S4**), indicating efficient charge carrier transport with minimal scattering. The combination of a relatively high $\mu\tau$ product and long diffusion length demonstrates the efficient charge carrier transport of 2D-$Cs_3Bi_2Br_3I_{5.2}$ MCs, as shown in **Table 2**, despite the presence of iodine vacancies. Further, photocurrent-voltage measurements under varying white light intensities (0.18 to 2.64 mW/cm^2) (see **Figure S19**) showed an increase in photocurrent with intensity. However, the $\mu\tau$ product decreased significantly with increasing intensity (see **Figure 6c**), as determined using the modified Hecht equation. Power-law fitting produced a factor of -0.85, indicating that the reduction in $\mu\tau$ is due to trap-assisted monomolecular recombination and carrier-carrier scattering.[67–69] These findings highlight the interplay between charge transport efficiency and recombination mechanisms in 2D- $Cs_3Bi_2Br_3I_{5.2}$ MCs.

Table 2: Carrier dynamics parameters of 2D $Cs_3Bi_2Br_3I_{5.2}$ MCs

Material	**V_{TFL} (V)**	**η_{trap} (cm^{-3})**	**μ ($cm^2V^{-1}s^{-1}$)**	**$\mu\tau$ (cm^2V^{-1})**	**L_D (µm)**
$Cs_3Bi_2Br_3I_{5.2}$	0.27	1.1×10^{11}	1.12	3.8×10^{-6}	3.08

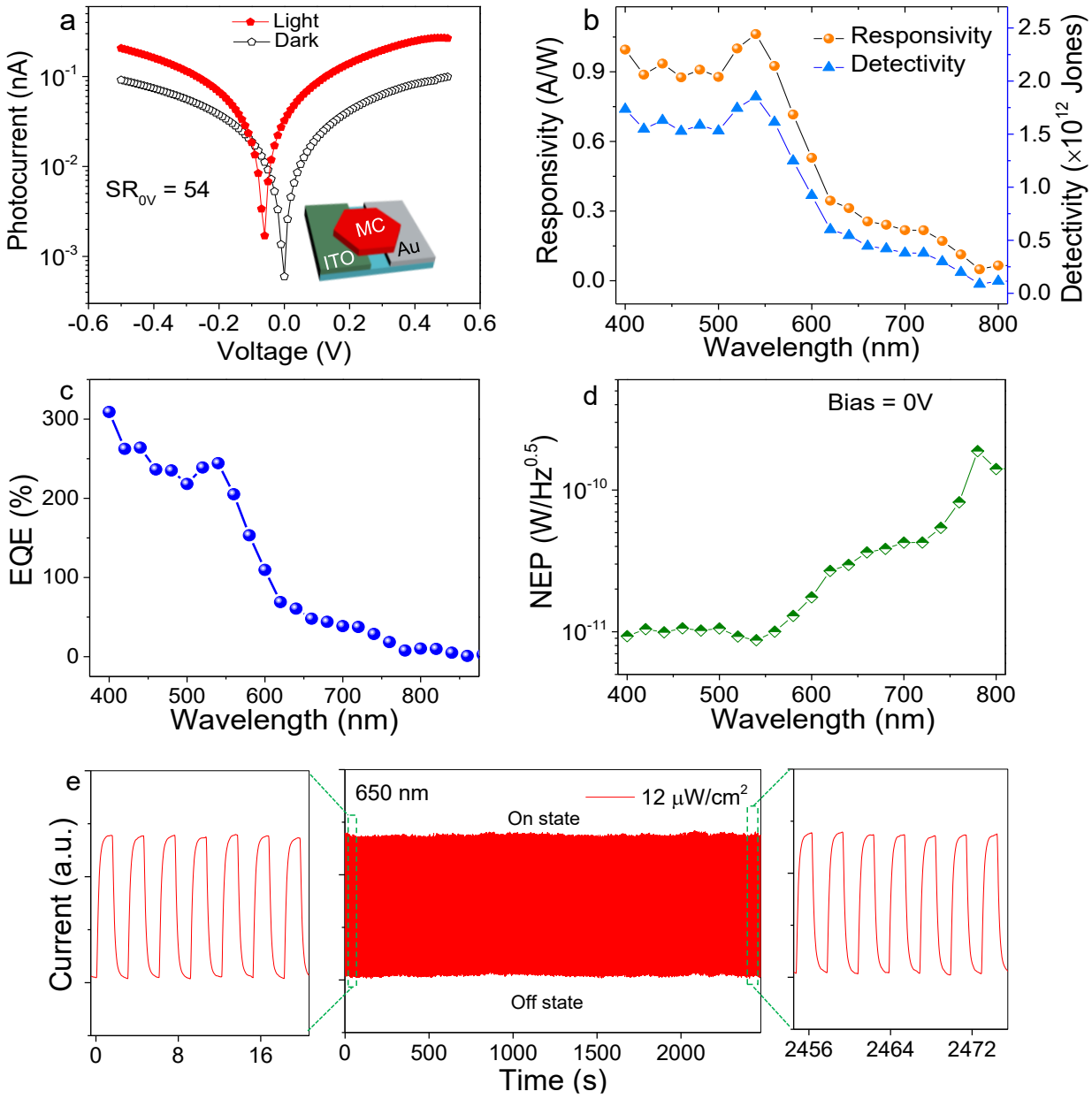

Figure 7. (a) Photocurrent and dark current (semi-logarithmic scale) of 2D-$Cs_3Bi_2Br_3I_{5.2}$ MC-based photodetectors as a function of voltage. Inset: Schematic diagram of the 2D-$Cs_3Bi_2Br_3I_{5.2}$ MC photodetector device. (b) Responsivity and detectivity of the 2D-$Cs_3Bi_2Br_3I_{5.2}$ MC photodetector. (c) External quantum efficiency (EQE) versus wavelength for the photodetector at 0 V applied bias. (d) Noise equivalent power (NEP) as a function of incident light wavelength (400–900 nm) for the self-powered photodetector. (e) Transient photocurrent stability of the photodetector under 824 on-off cycles at 0.3 Hz with 450 nm light illumination (12 μW/cm²).

The photodetector characteristics were evaluated using an asymmetric electrode configuration (ITO/MC/Au). Here, a single MC was placed on pre-fabricated electrodes via micro imprint

lithography (see **Experimental section**). The 2D-$Cs_3Bi_2Br_3I_{5.2}$ MC demonstrated self-powered behavior under white light illumination (1.72 mW/cm^2), achieving a photo-switching ratio (SR) of 54 at 0 V bias (**Figure 7a**). This self-powered characteristic is attributed to the differing work functions of the asymmetric electrodes.[70,71] All performance parameters of the photodetector were calculated as outlined in **Section S5**. The highest responsivity (R) was 0.9 A/W at 500 nm, decreasing to 0.2 A/W at 760 nm (**Figure 7b**), significantly surpassing the responsivity of other halide perovskite-based photodetectors (see **Table S11**). The $Cs_3Bi_2Br_3I_{5.2}$ MC exhibited dual photoresponse over the 400 to 800 nm wavelength range (**Figure 7b** and **Figure S20**). In the 400-600 nm region, enhanced photo-response is attributed to band-edge absorption, while in the 600-800 nm range, it corresponds to mid-gap states originating from iodine vacancies, supported by single crystal XRD, XPS, PL spectra, TAS and DFT calculations. The $Cs_3Bi_2Br_3I_{5.2}$ MC-based photodetector demonstrated consistent detectivity (D) of ~10^{12} Jones within the bandgap edge (400-600 nm) and ~ 10^{11} Jones up to 800 nm, extending beyond the bandgap (see **Figure 7b**). The external quantum efficiency (EQE) of 2D-$Cs_3Bi_2Br_3I_{5.2}$ MC was estimated to be 205 % at 560 nm (see **Figure 7c**). Additionally, the noise-equivalent power (NEP) for these MCs varied from 9.3 to 188 pW/Hz$^{0.5}$ across the 400-800 nm wavelength range (see **Figure 7d**). The enhanced NEP value of the 2D-$Cs_3Bi_2Br_3I_{5.2}$ MC is ascribed to low dark current and heightened sensitivity, enabling efficient detection of small light signals up to 104 nW/cm^2.[72] Moreover, the transient photocurrent stability, shown in **Figure 7e** and **Figure S21-S22**, demonstrated robust performance over 824 on-off cycles at 0.3 Hz under illumination with 650 nm (mid-gap excitation) and 450 nm (above-bandgap excitation) of light. Remarkably, the 2D-$Cs_3Bi_2Br_3I_{5.2}$ MC-based photodetector exhibits superior self-driven performance compared to other $A_3Bi_2I_9$-type halide perovskites (**Table S11**). Rather than degrading performance, iodine vacancies act as a tuneable element, modifying the

spectral response. The synergy between low exciton binding energy and high carrier mobility, facilitated by band alignment due to n-type doping from iodine vacancies, drives the enhanced photoresponse of the device.[26]

Table 3: Key Performance Metrics for 2D-$Cs_3Bi_2Br_3I_{5.2}$ Microcrystal Photodetectors

Material	SR_{0V}	$R^{a)}_{500nm}$ (A/W)	$D^{b)}_{500nm}$ (Jones)	EQE_{500nm} (%)	NEP_{500nm} ($pW/Hz^{0.5}$)	LDR (dB)	Rise/fall time (ms)
$Cs_3Bi_2Br_3I_{5.2}$	54.2	0.9	1.5×10^{12}	205	10.5	79.8	100/258

R^a = Responsivity, D^b = Detectivity

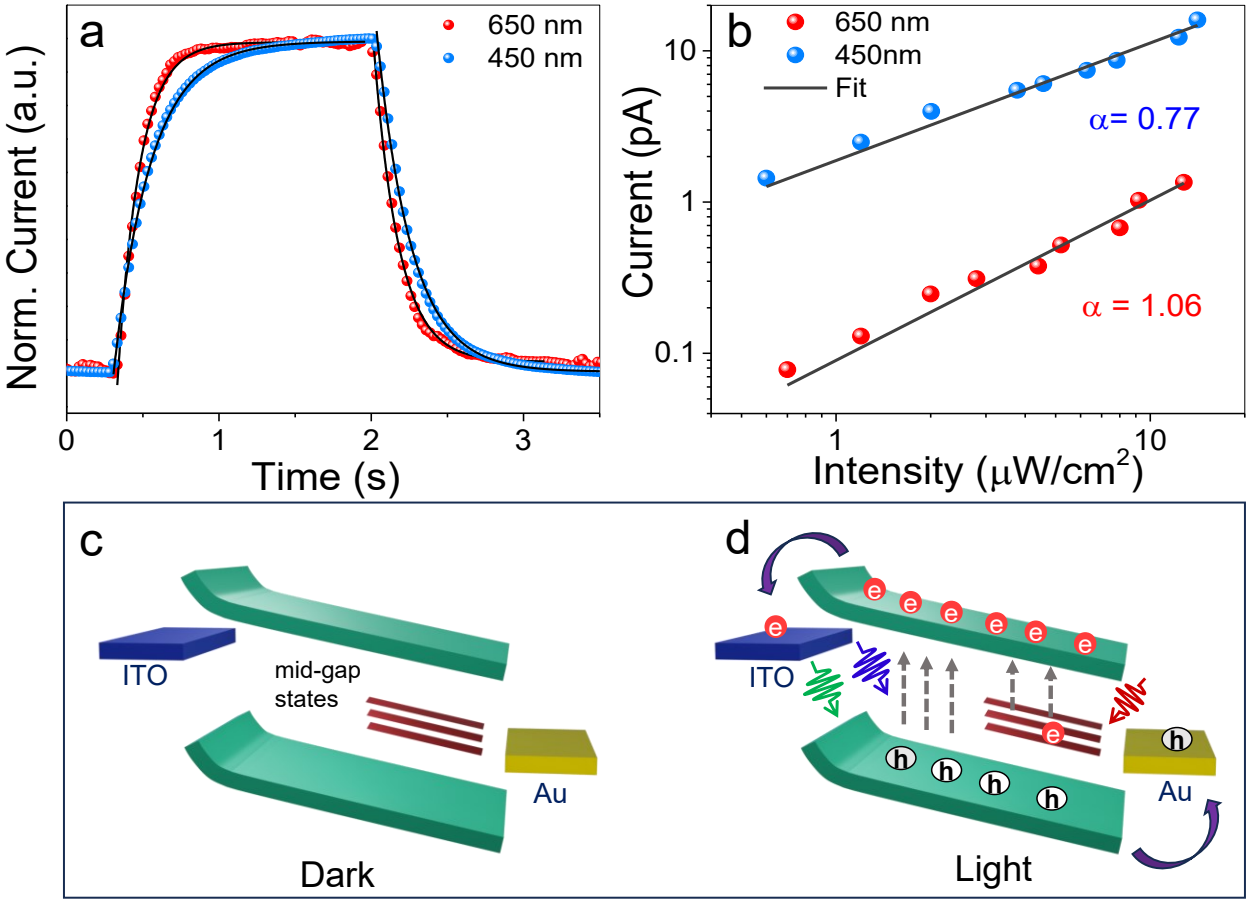

Figure 8. (a) Normalized photoresponse curves to estimate the rise and decay times of the device under illumination with 450 nm and 650 nm light sources. (b) Power-law fitting of photocurrent as a function of incident light intensity for 450 nm and 650 nm illumination. Schematic of the band diagram for the transportation of charge carriers in (c) dark, d) with illumination at 0 V bias.

To study the photo-absorption mechanism for mid-gap states, the $Cs_3Bi_2Br_3I_{5.2}$-based photodetector was tested under band edge (450 nm) and mid-gap excitation (650 nm). The device exhibited faster response times for 650 nm light (T_r = 144 ms, T_d = 163 ms) compared to 450 nm (T_r = 238 ms, T_d = 248 ms) (**Figure 8a** and **Table S12**). Photocurrent versus light intensity analysis (reduced χ^2 = 0.98) revealed power factors of 0.77 (sublinear) for 450 nm and 1.06 (linear) for 650 nm (**Figure 8b**). The sublinear behaviour at 450 nm is attributed to monomolecular trapping and carrier-carrier scattering due to the high absorption coefficient.[67–69] While the absence of significant recombination centers and the lower absorption coefficient for 650 nm light result in negligible scattering and a linear photocurrent response (α = 1.06). This also explains the faster response under 650 nm illumination compared to 450 nm, as shown in **Figure 8a**. Here, two-photon absorption (TPA), which generates quadratic photocurrent (α = 2),[73–75] was ruled out due to the observed linear response. Instead, the photo-assisted Shockley-Read-Hall (SRH) mechanism explains the linear behavior, where mid-gap photons excite carriers from deep levels into the CBM or VBM. [10,76] This mechanism, supported by the low absorption coefficient and electron-donating mid-gap states from iodine vacancies, aligns with the observed mid-gap photodetection in $Cs_3Bi_2Br_3I_{5.2}$.

The mechanism of the self-driven nature of 2D-$Cs_3Bi_2Br_3I_{5.2}$ MC-based photodetectors is illustrated in the band diagrams shown in **Figures 8c** to **8d**. This mechanism is driven by the built-in potential, which arises due to the mismatch in work functions between the two different metal/MC junctions (ITO and Au). When illuminated, this built-in potential facilitates the separation of photogenerated charge carriers without the need for an external bias. The effective band alignment enables the free transfer of these charges to the neighbouring electrode, significantly enhancing the photoresponse.[70] This self-driven photoresponse is attributed to the

asymmetric electrode configuration and presence of iodine vacancies in 2D-$Cs_3Bi_2Br_3I_{5.2}$ MCs, which is crucial for ultra-low-power light detection applications. In metal halide perovskites, mid-gap states play a role in phonon-to-electrical energy conversion through either electron transitions from the valence band (E_V) to mid-gap states (hole transition to E_V) or from mid-gap states to the conduction band (E_C).[30,77,78] For 2D-$Cs_3Bi_2Br_3I_{5.2}$, the latter mechanism dominates due to its n-type behaviour. Additionally, these mid-gap states become optically active, generating a photoresponse in self-bias mode under the influence of the internal electric field. The benign mid-gap states induced by iodine vacancies thus play a crucial role in improving the photophysical properties, making these MCs highly effective for advanced optoelectronic applications.

Conclusions

In conclusion, we have successfully synthesized facet-oriented 2D-$Cs_3Bi_2Br_3I_{5.2}$ MCs with iodine vacancies using an Ag-assisted modified hot-spin casting method. Structural analysis (SC-XRD) confirmed that these MCs crystallize in a trigonal crystal structure (P-3m1 space group), with iodine vacancies leading to a reduced unit cell volume compared to $Cs_3Bi_2Br_3I_6$. Charge density analysis revealed that iodine vacancies originate localized states around Bi atoms, significantly affecting the electronic properties. DFT analysis further confirmed that these vacancies introduce mid-gap states. The 2D-$Cs_3Bi_2Br_3I_{5.2}$ MCs exhibited an indirect bandgap of 2.03 eV, with no evidence of an excitonic absorption peak. The PL spectra showed a narrow emission peak at 605 nm with an insignificant Stokes shift, indicating emission predominantly from band edges. The corresponding lifetime extends into the nanosecond scale. The low exciton binding energy (92 meV) and reduced electron-phonon coupling (S=10) compared to other halide PIMs contribute to efficient charge carrier transport. SCLC analysis revealed low to moderate trap densities of 5×10^{11} cm^{-3} and carrier mobility of 1.12 $cm^2V^{-1}s^{-1}$. Under light illumination, the 2D-$Cs_3Bi_2Br_3I_{5.2}$ MCs

demonstrated promising self-driven photodetector characteristics with a responsivity of 0.9 A/W, highlighting their potential for high-performance optoelectronic devices. Notably, iodine vacancies do not degrade band-edge excitons but instead extend the spectral response beyond the bandgap. The mid-gap photodetection follows a photo-assisted Shockley-Read-Hall (SRH) mechanism, where mid-gap photons excite electrons from deep donor levels into the conduction band. These findings highlight the role of defect engineering in tuning optoelectronic properties in halide Bi-based perovskite-inspired materials (Bi-PIMs). The iodine vacancies provide a controlled way to modulate spectral response while maintaining stability and efficient charge transport. This work further emphasizes the potential of low-toxicity, vacancy-engineered PIMs for high-performance and environmentally sustainable light-harvesting applications.

Author contributions

K.S. and M.H. contributed to data curation, formal analysis, investigation, and methodology, as well as writing the original draft. S.K., A.V.M., and P.S. assisted with data curation, formal analysis, and investigation. P.R. and S.M. focused on formal analysis, investigation, and validation. P.K.N. and D.G. handled the investigation, methodology, and software development and contributed resources. K.V.A. and A.T. executed and analysed transient absorbance spectroscopy, G.K.G. and P.V. were involved in the investigation, writing, review, and editing. K.D.M.R. led the formal analysis, funding acquisition, investigation, methodology, project administration, and resource management while also overseeing supervision, validation, visualization, writing – review, and editing.

[ǂ] These authors contributed equally to this work

Corresponding Author
K. D. M. Rao
* E-mail: mallik2arjun@gmail.com, saiskdmrao@iacs.res.in

Conflicts of interest

Authors have no conflict of interest

Acknowledgments

K.S. acknowledges CSIR for fellowship and IACS for research facilities. M.H., S.K., and P.S. acknowledge UGC for fellowship. K.D.M.R. acknowledges the Science and Engineering Research Board (SERB) projects CRG/2022/004873 and UGC-DAE CRS/2022-23/01/676 projects for financial support. P.K.N acknowledges the Prime Minister's Research Fellowship (PMRF ID: 1402687). D.G. acknowledges the IIT Delhi SEED Grant (PLN12/04MS), the SERB, Department of Science and Technology (DST), India for Start-up Research Grant SRG/2022/00l234, CSIR-Human Resource Development Group (HRDG) for Extra Mural Research-II Grant 01/3136/23/EMR-II and the IIT Delhi HPC facility for computational resources. This work was performed, in part, at the Center for Integrated Nanotechnologies, an Office of Science User Facility operated for the U.S. Department of Energy (DOE) Office of Science by Los Alamos National Laboratory (Contract 89233218CNA000001) and Sandia National Laboratories (Contract DE-NA-0003525). K.V.A. and A.T. gratefully acknowledge the support from the Department of Science and Technology (DST), India, through the project DST/NM/TUE/QM-8/2019(G)/1. P.V. thanks Research Council of Finland, Decision No. 347772. The work is part of the Research Council of Finland Flagship Programme, Photonics Research and Innovation (PREIN), decision number 346511.

Note and Reference:

1 G. K. Grandhi, D. Hardy, M. Krishnaiah, B. Vargas, B. Al-Anesi, M. P. Suryawanshi, D. Solis-Ibarra, F. Gao, R. L. Z. Hoye and P. Vivo, *Adv. Funct. Mater.*, 2023, 2307441.

2 T. Li, S. Luo, X. Wang and L. Zhang, *Adv. Mater.*, 2021, **33**, 2008574 (1 of 30).

3 K. V. Seshaiah and J. H. Kim, *Chem. Eng. J.*, 2024, **492**, 152370.

4 J. Park, J. Kim, H. S. Yun, M. J. Paik, E. Noh, H. J. Mun, M. G. Kim, T. J. Shin and S. Il Seok, *Nature*, 2023, **616**, 724–730.

5 Y. K. Wang, F. Jia, X. Li, S. Teale, P. Xia, Y. Liu, P. T. S. Chan, H. Wan, Y. Hassan, M. Imran, H. Chen, L. Grater, L. D. Sun, G. C. Walker, S. Hoogland, Z. H. Lu, C. H. Yan, L. S. Liao and E. H. Sargent, *Sci. Adv.*, 2023, **9**, 1–9.

6 J. Ye, N. Mondal, B. P. Carwithen, Y. Zhang, L. Dai, X.-B. Fan, J. Mao, Z. Cui, P. Ghosh, C. Otero-Martínez, L. van Turnhout, Y.-T. Huang, Z. Yu, Z. Chen, N. C. Greenham, S. D. Stranks, L. Polavarapu, A. Bakulin, A. Rao and R. L. Z. Hoye, *Nat. Commun.*, 2024, **15**, 8120.

7 D. P. Nenon, K. Pressler, J. Kang, B. A. Koscher, J. H. Olshansky, W. T. Osowiecki, M. A. Koc, L.-W. Wang and A. P. Alivisatos, *J. Am. Chem. Soc.*, 2018, **140**, 17760–17772.

8 Z. Xiao, W. Meng, J. Wang, D. B. Mitzi and Y. Yan, *Mater. Horizons*, 2017, **4**, 206–216.

9 Y. Cui, L. Yang, X. Wu, J. Deng, X. Zhang and J. Zhang, *J. Mater. Chem. C*, 2022, **10**, 16629–16656.

10 M. Casalino, G. Coppola, M. Iodice, I. Rendina and L. Sirleto, *Sensors*, 2010, **10**, 10571–10600.

11 R. E. Brandt, J. R. Poindexter, P. Gorai, R. C. Kurchin, R. L. Z. Hoye, L. Nienhaus, M. W. B. Wilson, J. A. Polizzotti, R. Sereika, R. Žaltauskas, L. C. Lee, J. L. Macmanus-Driscoll, M. Bawendi, V. Stevanović and T. Buonassisi, *Chem. Mater.*, 2017, **29**, 4667–4674.

12 T. L. Hodgkins, C. N. Savory, K. K. Bass, B. L. Seckman, D. O. Scanlon, P. I. Djurovich, M. E. Thompson and B. C. Melot, *Chem. Commun.*, 2019, **55**, 3164–3167.

13 L. R. V. Buizza and L. M. Herz, *Adv. Mater.*, 2021, **33**, 2007057 (1 of 19).

14 S. R. Rondiya, R. A. Jagt, J. L. MacManus-Driscoll, A. Walsh and R. L. Z. Hoye, *Appl. Phys. Lett.*, 2021, **119**, 220501(1–11).

15 X. Zhu, J. Lee and W. D. Lu, *Adv. Mater.*, 2017, **29**, 1–8.

16 J. Ran, B. Wang, Y. Wu, D. Liu, C. Mora Perez, A. S. Vasenko and O. V. Prezhdo, *J. Phys. Chem. Lett.*, 2023, **14**, 6028–6036.

17 X. Feng, Y. Li, B. Liu, C. Tong, M. Long, M. Cai and J. Yang, *J. Phys. Chem. Lett.*, 2024, **15**, 2209–2215.

18 J. Zhang, X. Zhang, M. E. Turiansky and C. G. Van de Walle, *PRX Energy*, 2023, **2**, 013008.

19 D. Shi, V. Adinolfi, R. Comin, M. Yuan, E. Alarousu, A. Buin, Y. Chen, S. Hoogland, A. Rothenberger, K. Katsiev, Y. Losovyj, X. Zhang, P. A. Dowben, O. F. Mohammed, E. H. Sargent and O. M. Bakr, *Science (80-.).*, 2015, **347**, 519–522.

20 J. Xu, J. Liu, B. Liu, J. Wang and B. Huang, *Adv. Funct. Mater.*, 2019, **29**, 1805870 (1–11).

21 M. Hossain, M. S. Sheikh and K. D. M. Rao, *Adv. Mater. Interfaces*, 2021, **8**, 1–10.

22 R. A. Jagt, I. Bravić, L. Eyre, K. Gałkowski, J. Borowiec, K. R. Dudipala, M. Baranowski, M. Dyksik, T. W. J. van de Goor, T. Kreouzis, M. Xiao, A. Bevan, P. Płochocka, S. D. Stranks, F. Deschler, B. Monserrat, J. L. MacManus-Driscoll and R. L. Z. Hoye, *Nat.*

Commun., 2023, **14**, 2452.
23 A. D. Wright, L. R. V. Buizza, K. J. Savill, G. Longo, H. J. Snaith, M. B. Johnston and L. M. Herz, *J. Phys. Chem. Lett.*, 2021, **12**, 3352–3360.
24 A. H. Slavney, T. Hu, A. M. Lindenberg and H. I. Karunadasa, *J. Am. Chem. Soc.*, 2016, **138**, 2138–2141.
25 G. Longo, S. Mahesh, L. R. V. Buizza, A. D. Wright, A. J. Ramadan, M. Abdi-Jalebi, P. K. Nayak, L. M. Herz and H. J. Snaith, *ACS Energy Lett.*, 2020, **5**, 2200–2207.
26 A. H. Slavney, L. Leppert, A. Saldivar Valdes, D. Bartesaghi, T. J. Savenije, J. B. Neaton and H. I. Karunadasa, *Angew. Chemie*, 2018, **130**, 12947–12952.
27 Z. Zheng, H. Li, L. Hai, R. Ma, R. Liu, C. Zhai, Z. Sun, F. Wang, Y. Ma, Q. Xie, X. Lou, T. Zhai and F. Xia, *Adv. Funct. Mater.*, 2024, **34**, 1–10.
28 Z. Li, Y.-T. Huang, L. Mohan, S. J. Zelewski, R. H. Friend, J. Briscoe and R. L. Z. Hoye, *Sol. RRL*, 2022, **6**, 2200749 (1–9).
29 G. K. Grandhi, B. Al-Anesi, H. Pasanen, H. Ali-Löytty, K. Lahtonen, S. Granroth, N. Christian, A. Matuhina, M. Liu, A. Berdin, V. Pecunia and P. Vivo, *Small*, 2022, **18**, 2203768 (1 of 8).
30 E. Choi, Y. Zhang, A. M. Soufiani, M. Lee, R. F. Webster, M. E. Pollard, P. J. Reece, W. Lee, J. Seidel, J. Lim, J.-H. Yun and J. S. Yun, *npj 2D Mater. Appl.*, 2022, **6**, 43.
31 M. Daum, S. Deumel, M. Sytnyk, H. A. Afify, R. Hock, A. Eigen, B. Zhao, M. Halik, A. These, G. J. Matt, C. J. Brabec, S. F. Tedde and W. Heiss, *Adv. Funct. Mater.*, 2021, **31**, 2102713 (1 of 10).
32 D. Liu, B.-B. Yu, M. Liao, Z. Jin, L. Zhou, X. Zhang, F. Wang, H. He, T. Gatti and Z. He, *ACS Appl. Mater. Interfaces*, 2020, **12**, 30530–30537.
33 J. Shi, Y. Li, Y. Li, D. Li, Y. Luo, H. Wu and Q. Meng, *Joule*, 2018, **2**, 879–901.
34 M. Hossain, M. S. Sheikh and K. D. M. Rao, *Adv. Mater. Interfaces*, 2021, **8**, 1–10.
35 S. Sun, M. Lu, X. Gao, Z. Shi, X. Bai, W. W. Yu and Y. Zhang, *Adv. Sci.*, 2021, **8**, 1–23.
36 R. A. Evarestov, A. Senocrate, E. A. Kotomin and J. Maier, *Phys. Chem. Chem. Phys.*, 2019, **21**, 7841–7846.
37 D. Meggiolaro, E. Mosconi and F. De Angelis, *ACS Energy Lett.*, 2019, **4**, 779–785.
38 H. Xue, J. M. Vicent-Luna, S. Tao and G. Brocks, *J. Phys. Chem. C*, 2023, **127**, 1189–1197.
39 K. M. McCall, C. C. Stoumpos, O. Y. Kontsevoi, G. C. B. Alexander, B. W. Wessels and M. G. Kanatzidis, *Chem. Mater.*, 2019, **31**, 2644–2650.
40 Y. Zhang, Y. Liu, Z. Xu, H. Ye, Z. Yang, J. You, M. Liu, Y. He, M. G. Kanatzidis and S. (Frank) Liu, *Nat. Commun.*, 2020, **11**, 1–11.
41 M. Gao, C. Zhang, L. Lian, J. Guo, Y. Xia, F. Pan, X. Su, J. Zhang, H. Li and D. Zhang, *J. Mater. Chem. C*, 2019, **7**, 3688–3695.
42 H. Wu, W. Liu, W. Ma, T. Liang, X. Liu and J. Fan, *Appl. Phys. Lett.*, 2022, **121**, 181902 (1–7).
43 A. Biswas, A. J. E. Rowberg, P. Yadav, K. Moon, G. J. Blanchard, K. E. Kweon and S. Kim, *J. Am. Chem. Soc.*, 2024, **146**, 19919–19928.
44 N. Droseros, D. Tsokkou and N. Banerji, *Adv. Energy Mater.*, 2020, **10**, 1–17.
45 I. Levine, D. Menzel, A. Musiienko, R. MacQueen, N. Romano, M. Vasquez-Montoya, E. Unger, C. Mora Perez, A. Forde, A. J. Neukirch, L. Korte and T. Dittrich, *J. Am. Chem. Soc.*, 2024, **146**, 23437–23448.
46 R. Jaramillo, M. J. Sher, B. K. Ofori-Okai, V. Steinmann, C. Yang, K. Hartman, K. A.

Nelson, A. M. Lindenberg, R. G. Gordon and T. Buonassisi, *J. Appl. Phys.*, 2016, **119**, 035101(1–16).
47 J. A. Vigil, N. R. Wolf, A. H. Slavney, R. Matheu, A. Saldivar Valdes, A. Breidenbach, Y. S. Lee and H. I. Karunadasa, *ACS Cent. Sci.*, 2024, **10**, 907−919.
48 Z. Xiao, Y. Zhou, H. Hosono and T. Kamiya, *Phys. Chem. Chem. Phys.*, 2015, **17**, 18900–18903.
49 Z. Xiao, W. Meng, J. Wang and Y. Yan, *Phys. Chem. Chem. Phys.*, 2016, **18**, 25786–25790.
50 G. M. Paternò, N. Mishra, A. J. Barker, Z. Dang, G. Lanzani, L. Manna and A. Petrozza, *Adv. Funct. Mater.*, 2019, **29**, 1–6.
51 P. Maity, S. Satapathi and N. K. Tailor, *J. Phys. Chem. Lett.*, 2022, **13**, 5260–5266.
52 H. Lei, D. Hardy and F. Gao, *Adv. Funct. Mater.*, 2021, **31**, 2105898.
53 S. Yang, S. Huang, Q. Wang, R. Wu, Q. Han and W. Wu, *Opt. Mater. (Amst).*, 2019, **98**, 109444.
54 J.-P. Correa-Baena, L. Nienhaus, R. C. Kurchin, S. S. Shin, S. Wieghold, N. T. Putri Hartono, M. Layurova, N. D. Klein, J. R. Poindexter, A. Polizzotti, S. Sun, M. G. Bawendi and T. Buonassisi, *Chem. Mater.*, 2018, **30**, 3734–3742.
55 K. M. McCall, C. C. Stoumpos, S. S. Kostina, M. G. Kanatzidis and B. W. Wessels, *Chem. Mater.*, 2017, **29**, 4129–4145.
56 S. Rieger, B. J. Bohn, M. Döblinger, A. F. Richter, Y. Tong, K. Wang, P. Müller-Buschbaum, L. Polavarapu, L. Leppert, J. K. Stolarczyk and J. Feldmann, *Phys. Rev. B*, 2019, **100**, 201404.
57 T. Kawai and S. Shimanuki, *Phys. status solidi*, 1993, **177**, K43–K45.
58 R. L. Z. Hoye, J. Hidalgo, R. A. Jagt, J. Correa-Baena, T. Fix and J. L. MacManus-Driscoll, *Adv. Energy Mater.*, 2022, **12**, 2100499 (1–59).
59 J. Pradhan, A. Das, A. Panda and K. Biswas, *Chem. Mater.*, 2024, **36**, 3405–3416.
60 A. D. Wright, C. Verdi, R. L. Milot, G. E. Eperon, M. A. Pérez-Osorio, H. J. Snaith, F. Giustino, M. B. Johnston and L. M. Herz, *Nat. Commun.*, 2016, **7**, 11755.
61 J. C. Blakesley, F. A. Castro, W. Kylberg, G. F. A. Dibb, C. Arantes, R. Valaski, M. Cremona, J. S. Kim and J. S. Kim, *Org. Electron.*, 2014, **15**, 1263–1272.
62 M. Bouzidi, M. Ben Bechir, D. R. Almalawi, I. H. Smaili, F. Aljuaid and N. I. Aljuraide, *Opt. Mater. (Amst).*, 2024, **154**, 115640.
63 V. M. Le Corre, E. A. Duijnstee, O. El Tambouli, J. M. Ball, H. J. Snaith, J. Lim and L. J. A. Koster, *ACS Energy Lett.*, 2021, **6**, 1087–1094.
64 X. Li, G. Zhang, Y. Hua, F. Cui, X. Sun, J. Liu, H. Liu, Y. Bi, Z. Yue, Z. Zhai, H. Xia and X. Tao, *Angew. Chemie Int. Ed.*, 2023, **62**, e202315817.
65 Y. Zhang, Y. Liu, Z. Xu, H. Ye, Z. Yang, J. You, M. Liu, Y. He, M. G. Kanatzidis and S. (Frank) Liu, *Nat. Commun.*, 2020, **11**, 2304.
66 J. A. Röhr and R. C. I. MacKenzie, *J. Appl. Phys.*, 2020, **128**, 165701(1–10).
67 X. Meng, Y. Du, W. Wu, N. B. Joseph, X. Deng, J. Wang, J. Ma, Z. Shi, B. Liu, Y. Ma, F. Yue, N. Zhong, P.-H. Xiang, C. Zhang, C.-G. Duan, A. Narayan, Z. Sun, J. Chu and X. Yuan, *Adv. Sci.*, 2023, **10**, 2300413.
68 D. H. Kang, M. S. Kim, J. Shim, J. Jeon, H. Y. Park, W. S. Jung, H. Y. Yu, C. H. Pang, S. Lee and J. H. Park, *Adv. Funct. Mater.*, 2015, **25**, 4219–4227.
69 J. Ghosh, L. P. L. Mawlong, G. B. Manasa, A. J. Pattison, W. Theis, S. Chakraborty and P. K. Giri, *J. Mater. Chem. C*, 2020, **8**, 8917–8934.

70 C. Perumal Veeramalai, S. Yang, R. Zhi, M. Sulaman, M. I. Saleem, Y. Cui, Y. Tang, Y. Jiang, L. Tang and B. Zou, *Adv. Opt. Mater.*, 2020, **8**, 1–9.

71 J. Ding, H. Fang, Z. Lian, J. Li, Q. Lv, L. Wang, J.-L. Sun and Q. Yan, *CrystEngComm*, 2016, **18**, 4405–4411.

72 S. Bansal, K. Sharma, P. Jain, N. Sardana, S. Kumar, N. Gupta and A. K. Singh, *RSC Adv.*, 2018, **8**, 39579–39592.

73 F. Zhou, I. Abdelwahab, K. Leng, K. P. Loh and W. Ji, *Adv. Mater.*, 2019, **31**, Adv. Mater. 2019, 31, 1904155 1904155.

74 J. Song, Q. Cui, J. Li, J. Xu, Y. Wang, L. Xu, J. Xue, Y. Dong, T. Tian, H. Sun and H. Zeng, *Adv. Opt. Mater.*, 2017, **5**, 1700157.

75 J. Chen, W. Zhang and T. Pullerits, *Mater. Horizons*, 2022, **9**, 2255–2287.

76 B. Vest, E. Lucas, J. Jaeck, R. Haïdar and E. Rosencher, *Appl. Phys. Lett.*, 2013, **102**, 031105–1.

77 J. Wu, Y. Miao, X. Qi, L. Yang, X. Wang, F. Zheng, F. Zhao, Z. Zhao, S. Shafique, H. Zhang and Z. Hu, *J. Mater. Chem. A*, 2024, **12**, 20425–20436.

78 Q. Lin, A. Armin, P. L. Burn and P. Meredith, *Laser Photon. Rev.*, 2016, **10**, 1047–1053.